

Characterization of Josephson Junction Aging and Annealing Under Different Environments

Rangga P. Budoyo,^{1,*} Rasanayagam S. Kajen,¹ Cheah Bing Wen,² Long H. Nguyen,² and Rainer Dumke^{2,1,†}

¹*Centre for Quantum Technologies, National University of Singapore, 3 Science Drive 2, Singapore 117543, Singapore*

²*Division of Physics and Applied Physics, School of Physical and Mathematical Sciences, Nanyang Technological University, 21 Nanyang Link, Singapore 637371, Singapore*

Understanding the aging behavior of Josephson junctions and the effect of annealing on junction resistances is important in building large-scale superconducting quantum processors. Here we study the effects of aging of Al/AlO_x/Al Josephson junctions under different storage conditions from immediately after fabrication up to 2 to 3 months. We find that the aging curve follows a logarithmic curve, with the aging amplitude mainly determined by fabrication conditions and the aging speed determined by storage conditions. Junctions stored at ambient laboratory conditions aged faster compared to junctions stored in a nitrogen atmosphere or vacuum, with the aging speed appreciably changes when the storage condition changed. We also compared the effect of thermal annealing under nitrogen environment with annealing under ambient conditions up to 250°C. We find that under nitrogen environment, the resistances decreased at all temperatures tested, while under ambient environment the resistances increased at 200°C and decreased at 250°C instead. We were unable to decrease the resistance below the initial-time resistance, suggesting a lower limit on the range of resistance tuning.

I. INTRODUCTION

Josephson junctions are essential elements in superconducting quantum processors [1, 2]. For all types of superconducting qubits, their frequencies depend on the critical current I_c of the junctions, which in turn depends on fabrication conditions including the junction area and oxidation parameters. At room temperature, I_c can be estimated by measuring the junction resistance R , which is related to I_c via the Ambegaokar-Baratoff relation [3]. For large-scale quantum processors, precise and accurate junction fabrication is important for qubit frequency assignment to avoid frequency collisions that can limit qubit gate performance [4, 5]. Current state-of-the-art fabrication performance gives about 3% wafer-scale I_c coefficient-of-variation (CV) and 1-2% chip-scale I_c CV [6–8].

To improve the frequency accuracy, several junction anneal methods that change the critical current post-fabrication are developed. These include thermal annealing (i.e heating), which has been reported to decrease I_c (increase R) or increase I_c (decrease R) depending on the temperature and the heating environment [9–11]. However, thermal annealing is limited to chip-scale adjustment only, while junction-scale annealing will be necessary for frequency accuracy improvement. In recent years, laser annealing [4, 12, 13], electron-beam annealing [14], and voltage annealing [15–17] are developed that allows junction-scale tuning, although they are so far limited to decreasing I_c .

An additional factor that needs to be taken into account is the fact that the junctions “aged”, where the

resistance slowly increased over time [10, 18]. As a result, a qubit’s measured frequency can differ significantly from its expected frequency if its R is measured significantly before it is cooled down. Recent reports show that junction aging is affected by junction design and fabrication, including junction dimensions and oxidation parameters [19]. Several methods have been shown to inhibit aging, including plasma cleaning [20], additional oxidation steps [21], or using etching instead of lift-off process [22]. However, reducing the aging appears to also reduce the junction sensitivity to annealing [19, 21], suggesting a balance between the two is needed in the manufacturing of large scale quantum processors.

In this work, we study the Al/AlO_x/Al junction aging properties under different storage environments over several months, including ambient atmosphere, nitrogen glove box, and vacuum. We observed that aging speed mainly depend on the storage conditions, with ambient conditions resulted in fastest aging. On the other hand, the aging amplitude appears to be limited mainly by fabrication conditions, similar to recent reports [19]. Changing the storage conditions of the chips results in an apparent change in aging speed, with a resistance decrease (\equiv junction “deaging”) observed when the junctions are moved from ambient atmosphere to glove box. We also studied the effect of prior storage on both voltage annealing and thermal annealing of Josephson junctions. The results from voltage annealing experiments suggest this process did not induce an accelerated aging of junctions, but instead changed the internal structure of the junctions. For thermal annealing in nitrogen atmosphere, we only observed decrease in R up to 250° C temperatures, consistent with previous reports in low-oxygen environment [9, 11]. For thermal annealing in ambient conditions, we observed increase in R for 200° C and decrease in R for 250° C. Additionally, the lower limit for resistance decrease appeared to be the initial (immediately

* cqtrpb@nus.edu.sg

† rdumke@ntu.edu.sg

after fabrication) R value. Understanding junction aging and annealing characteristics allows one to plan the optimal storage and the timing and annealing method for different resistance targets.

II. EXPERIMENTAL DETAILS

The test Al/AlO_x/Al junctions used in this work were fabricated using the Dolan junction fabrication procedure widely used in the fabrication of superconducting qubits [23, 24]. Each test chip consists of 16 junctions, with a typical fabricated size of approximately 250 nm × 250 nm.

High-resistivity silicon wafers (> 10000 Ω cm) are diced into individual 1.5 cm × 1.5 cm square chips. We spin-coated bilayer e-beam resist, consisting of 500 nm MMA-EL9 and 300 nm PMMA-A4-950K. After drawing the test junction patterns using e-beam lithography, the chips are developed using MIBK:IPA 1:3 solution for 40 s, and then loaded into the e-beam deposition system.

Before deposition, we performed in-situ cleaning and SiO₂ removal using a gentle argon ion mill (beam voltage 250 V) [25] at +60° and 0° tilt angles. A small flow of oxygen (Ar flow 9 sccm, O₂ flow 0.9 sccm) is included to remove organic residue. Two layers of Al are deposited with 0.5 nm/s rate, with different thicknesses and deposition tilt angles: 1st layer 60 nm and +60°, and 2nd layer 100 nm and 0°. We performed an oxidation step between the deposition of the 2 layers, with 0.5 mbar oxygen pressure and varying duration depending on target resistance. After the second deposition, we performed a final protective oxidation step for 10 mbar and 10 minutes. We performed liftoff using heated acetone (about 50°C) for approximately 45 minutes. This liftoff duration was shorter than the typical duration (several hours or overnight) so that we can measure the junction resistance as close to the deposition time as possible. We also did not perform additional bandage layer fabrication [26]. As a result, after the junction deposition the chips were not exposed to any baking step that may result in any significant thermal annealing. The initial resistance measurement of test junctions are typically done within 20 minutes after the end of lift-off (corresponding to about 4 hours after oxidation step), then the chips are stored in their assigned environment.

The chips are stored in a gel box, either in ambient atmosphere on a cupboard shelf in a (non-clean room) laboratory room with typical temperature of 22-23° C and relative humidity of about 60%, or inside a nitrogen glove box with 0.0% measured O₂ population, typical temperature of 19-20° C, and 1% or less relative humidity. One of the chips was temporarily stored inside the high-vacuum space of the e-beam deposition chamber used in the junction fabrication with a base pressure of $\sim 1 \times 10^{-7}$ mbar. As the probe station was located in ambient lab environment, during the resistance measurements the chips would need to be taken out of their

storage for approximately 20 minutes. Table I shows a summary of the storage conditions of the chips reported in this work. For 5 of the 6 chips, the initial resistance CV are between 3 and 6%. For Chip 6, the higher CV is because of a lower fabrication yield, with a region of open junctions.

Junction resistance measurement and voltage annealing are done using a semi-automated probe station system. To measure the resistance, we sweep the applied current between -25 nA and +25 nA while measuring the voltage across the junction, with the resistance given by the slope of the I - V curve. To voltage anneal the junction, we follow a similar procedure as the alternating bias assisted annealing (ABAA) method [15, 16]. We applied a sequence of alternating voltage pulses with typical ± 0.9 V amplitude and 1 s duration. A heating element allows us to heat the chips up to about 75° C, but for the junctions reported in this work, all the voltage annealing were done at room temperature.

Thermal annealing was performed using a reflow oven with a maximum temperature of 280° C, either in a nitrogen environment (< 1% measured O₂ population just outside the oven during the process) or in an ambient environment ($\approx 21\%$ O₂ population). The anneal process takes 8 minutes, with 3 minutes heating time to the specified temperature, 2 minutes hold time, and 3 minutes of cooling time. Afterwards, the chip was left in the oven for some time (typically about 10 minutes) for thermalization before the resistance was measured.

III. COMPARISON OF AGING BETWEEN DIFFERENT ENVIRONMENTS

A. Single Environment Chips

The resistances of junctions on Chip 1 (stored in ambient atmosphere) and Chip 2 (stored in glove box), which were simultaneously deposited, were measured over a period of 56 days. Fig. 1(a) shows the individual and averaged resistance of the test junctions during the measurement period, with $t = 0$ defined as approximately the time the chips are taken out from the acetone bath at the end of lift-off. Fig. 1(b) show the resistance CV of the resistances over the measurement period. For Chip 1 it grew slowly to about 7%, while for Chip 2 it remained about the same.

We fit the average and individual resistances to a phenomenological logarithmic fit [17]

$$\frac{R(t)}{R(t \approx 0)} = 1 + a \log \left[\frac{t}{\tau} + b \right] \quad (1)$$

where a corresponds to the fractional aging amplitude, τ corresponds to aging speed. We include an offset parameter b inside the logarithm to ensure the value remains finite at $t = 0$, and we expect $b \approx 1$ since the argument of the logarithm should approach unity at early times. Table II shows the fit parameters of the average resistance

Fabrication	Chip name	$\langle R \rangle(t \approx 0)$ (k Ω)	Storage	Anneal
1	Chip 1	$22.8 \pm 4.8\%$	Ambient Atmosphere	Voltage
	Chip 2	$24.3 \pm 5.9\%$	Nitrogen glove box	
2	Chip 3	$7.5 \pm 3.9\%$	Atmosphere and glove box (Alternating with Chip 4)	Thermal
	Chip 4	$8.7 \pm 5.1\%$	Glove box and atmosphere (Alternating with Chip 3)	
3	Chip 5	$11.1 \pm 3.3\%$	Vacuum for 7 days, then glove box	None
	Chip 6	$11.1 \pm 12.1\%$	Nitrogen glove box	

TABLE I. Summary of test chips reported in this work.

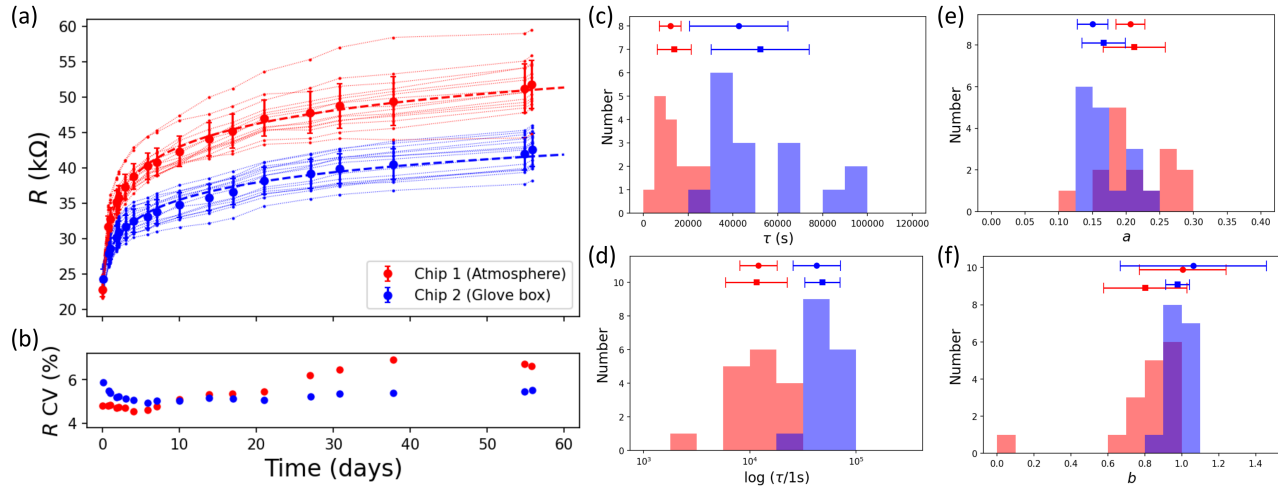


FIG. 1. Aging curves for test junctions stored in atmosphere and glove box. (a) Resistance R of test junctions over a period of 56 days. The small dots are the resistances of individual junctions, and the larger dots corresponds to the average resistance. The thick dashed lines are fit of the average resistances to logarithmic function of Eq. 1. (b) Resistance CV over the measurement period. (c-f) Histogram of fit parameters (c) τ (d) $\log(\tau)$ (e) a (f) b for each individual junction. The circle symbols correspond to the fit parameters obtained from the average resistance, while the square symbols correspond to the average value of the histogram.

for the 3 chips, as well as the average of the fit parameters from individual fits for each junction on each chip. The distribution of the individual junction fit parameters is shown in Fig. 1(c-f). As τ is located within the logarithmic term of Eq. 1 and the histogram showed an asymmetric distribution in Fig. 1(c), it is reasonable to show the distribution of $\log(\tau)$ instead [Fig. 1(d)]. The histograms for parameters a and b show some overlap for chips 1 and 2, while $\log(\tau)$ only show minimal overlap.

In Table II we also included the fit parameters obtained from the junctions in Chip 6 (in glove box) and the first 7 days of Chip 5 (while stored in vacuum). The junctions on both chips were also deposited simultaneously. The b parameters for all chips were all ≈ 1 , consistent with the expected value. The parameter a for Chips 5 and 6 are similar, and smaller than a for Chips 1 and 2. Conversely, τ for Chip 6 is close to the value for Chip 2, which has the same storage conditions, while for Chip 5 it was higher, indicating slower aging. Thus, we can infer that the aging amplitude (corresponding to a) mainly depend on the fabrication condition, similar to recent reports [19]. Meanwhile, the aging speed (corresponding to τ) mainly depends on the storage condition. The slightly

different value of τ between Chips 2 and 6 suggests fabrication also contributes to aging speed. τ in ambient conditions is about 3 to 4 times faster than in glove box, and about 5 times faster than in vacuum.

B. Alternating Environment Chips

Chip 3 was initially stored in atmosphere while Chip 4 was initially stored in glove box. Their junction resistances were measured over a period of about 85 days, with their storage condition swapped several times during this period. The fractional aging are shown in Fig. 2(a). As the chips are swapped, the apparent aging speed changed significantly. When the chips were moved from glove box to atmosphere, the chips aged more rapidly. When the chips were moved from atmosphere into glove box instead, the aging slowed significantly. When this swapping happens after $t \approx 4$ days, we observed a slight initial R decrease (“deaging”) instead. After the last swapping at $t = 12$ days, we observed no apparent aging for more than 40 days, with average resistance change of only about 1% during this period.

Parameter	Chip 1 (Atmosphere)	Chip 2 (Glove box)	Chip 6 (Glove box)	Chip 5 (Vacuum)
Duration	56 days	56 days	46 days	First 7 days
a	0.21 ± 0.02 0.21 ± 0.05	0.15 ± 0.02 0.17 ± 0.03	0.11 ± 0.06 0.10 ± 0.02	0.12 ± 0.06 0.12 ± 0.02
τ (10^4 s)	1.2 ± 0.5 1.4 ± 0.8	4.3 ± 2.2 5.2 ± 2.2	3.9 ± 6.8 3.2 ± 1.6	6.9 ± 6.5 6.1 ± 2.6
b	1.01 ± 0.23 0.80 ± 0.22	1.06 ± 0.39 0.98 ± 0.06	0.98 ± 1.09 0.78 ± 0.14	0.97 ± 0.26 0.92 ± 0.03

TABLE II. Fit values for junction resistances to Eq. 1. The upper column values are fit from the average resistance, and the lower values are the average values from individual fit for each junction.

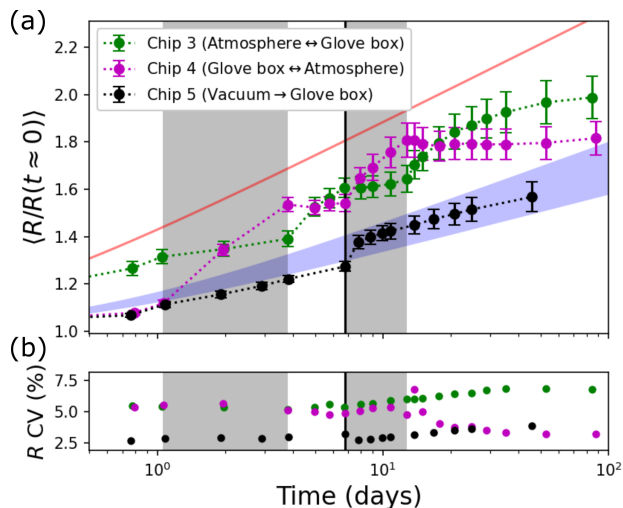


FIG. 2. (a) Average fractional aging of Chips 3, 4 and 5 in semilogarithmic axes. Chip 3 was stored in glove box while Chip 4 was stored in atmosphere during the shaded period, and vice versa during the non-shaded period. The black vertical line corresponds to the time Chip 5 was moved from vacuum to glove box. The red line and blue region correspond to the estimated aging bounds based on aging of Chips 1, 2 and 6. (b) Resistance CV over the measurement period.

The fractional aging of Chips 3 and 4 appears to be bounded by the expected aging fully in atmosphere and fully in glove box. These bounds are shown as the red line and blue regions in Fig. 2 and based on the aging curve of Chips 1, 2, and 6. As we showed in the previous section, the amplitude of the aging varied depending on the chip/fabrication and so the exact bound can vary between chips. The relaxation of the resistance towards these bounds appear to be quite slow, with apparent decay time of order several days.

Chip 5 was stored in high vacuum for the first 7 days. As Chip 5 was moved to the glove box, with the increase in oxygen pressure, we would expect a gradual increase in aging similar to Chips 3 and 4. Instead, as shown in Fig. 2(a), there appeared to be a more rapid relaxation (less than 1 day) towards the faster aging curve, and the

subsequent aging were within the expected aging in glove box.

Fig. 2(b) shows the resistance CV for the 3 chips. For Chip 5 it remained relatively constant during the entire period. For Chip 3 it increased slowly, especially after the last sample swap to atmosphere. Considering the increase in CV we observed for Chip 1, this would be expected. Surprisingly, for Chip 4, after the last swap it decreased gradually to about 3% when we would have expected it to remain constant.

IV. ANNEALING RESULTS

A. Alternating Bias Voltage Annealing

Chip	Voltage Anneal	$\langle \Delta R \rangle$ (k Ω)	$\langle \Delta R/R \rangle$ (%)	τ (10^4 s)
1	yes	7.4 ± 1.0	14.2 ± 1.0	5.0
	no	0.07 ± 0.07	0.1 ± 0.1	-
2	yes	7.6 ± 0.4	18.1 ± 1.4	1.6
	no	0.17 ± 0.06	0.4 ± 0.2	1.8

TABLE III. Average resistance change and aging/relaxation characteristic time after junction voltage annealing.

After the aging measurements described in Section III A, at $t = 56$ days after junction deposition, we annealed half of the junctions on Chips 1 and 2 using the ABAA annealing method at room temperature [15, 16], with 30 total square pulses (15 positive, 15 negative), each with 0.9 V amplitude and 1 s duration. Table III summarizes the effect of annealing process on the junctions. The non-annealed junctions were not affected by the annealing of nearby junctions. The annealed junctions on both chips increased by an average of approximately 7.5 k Ω , which corresponds to about 14% resistance increase for Chip 1 and about 18% increase for Chip 2.

Afterwards, we measured the post-annealed resistances for another 6 days, as shown in Fig. 3. For the non-annealed junctions on Chip 1, their resistances follow

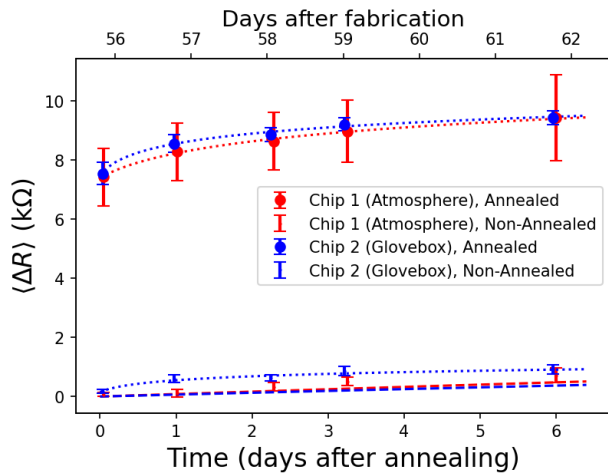


FIG. 3. Resistance change of the test junctions as a function of time after the voltage annealing process. The dashed lines correspond to the expected aging of the non-annealed junctions, extrapolated based on the fit parameters in Table III. The dotted lines correspond to the fit of the resistance drift to the logarithmic function of Eq. 1

the expected resistance (red dashed line, extrapolated to $t \gtrsim 56$ days based on fit parameters in Table II), while there was a small increase for Chip 2. This is likely due to the fact that during the annealing process, the chip was out in atmosphere for approximately 90 minutes, 4 to 5 times longer than the typical time it was in the atmosphere during the aging measurements in the previous section, and was under an accelerated aging for a short period. The annealed junctions on both chips follow a similar resistance curve, with initial apparent aging before slowing down after several days, similar to previous reports [16, 19]. We fit the resistances of the annealed junctions and the resistances of the non-annealed junctions of Chip 2 to the same logarithmic function of Eq. 1, with $t = 0$ defined as the voltage annealing time. Table III also shows the characteristic time τ from the fit, although we expect significant uncertainty due to relatively limited data. That τ values differ from the post-fabrication time (Table II) suggests that they do not correspond to aging speed, but possibly relaxation towards a bound curve (see Section IIIB), which, for very aged junctions, can be considered almost constant for several days.

B. Thermal Annealing

After the aging measurements described in Section IIIB, at $t \approx 85$ days, we performed thermal annealing on Chip 3 (stored in ambient atmosphere for about 70 days) and Chip 4 (stored in glove box for the same amount of time). The annealing for each chip was done at different days, but follow the exact same sequence as shown in Table IV. After each step, we measured the

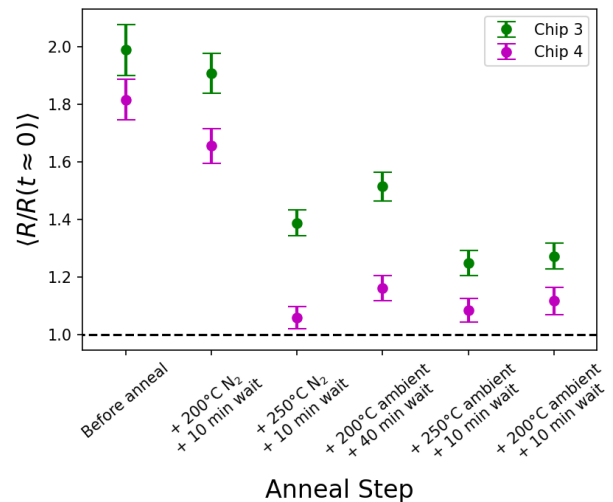


FIG. 4. Fractional resistance of the test junctions after each thermal annealing process. The horizontal dashed line corresponds to the $t \approx 0$ resistance value.

Step	Temperature (°C)	Environment	Wait time (minutes)
1	200	N ₂	10
2	250	N ₂	10
3	200	ambient	40
4	250	ambient	10
5	200	ambient	10

TABLE IV. Thermal annealing steps performed on Chips 3 and 4.

junction resistances, shown in Fig. 4. From the results, we can infer the following:

1. We observed no difference in the general annealing behavior between the chips.
2. For annealing in N₂, the resistances decreased for the temperatures used, with a larger decrease for 250° C. This is consistent with previous reports for thermal annealing in low-oxygen environment, either in forming gas (H₂/N₂ mixture) [9] or in argon [11].
3. For annealing in ambient atmosphere, we observed a resistance increase for annealing at 200° C, and a resistance decrease at 250° C. The decrease at 250° C was smaller than the decrease for the same temperature in N₂ atmosphere. The decrease at higher temperatures appear to show a reverse effect compared to thermal annealing at low-oxygen environments, where R increase emerged at high temperatures 400° C and above instead [9, 11].
4. Even though steps 3 and 5 have the exact same annealing process, we observed a slightly higher resistance increase for step 3. This is likely due to

the natural junction aging caused a further increase during the additional 30 minutes of thermalization.

5. We were unable to decrease the resistance to below the initial value, i.e. we could not deage the junctions to a $t < 0$ time. Thus, the minimum tuning range of junction resistance appeared to be set by the initial resistance, although this would require further study.

V. MICROSCOPIC PICTURE OF RESISTANCE AGING AND ANNEALING

At room temperature, the resistance reported in this work is the small-bias normal-state tunnel resistance of an Al/AlO_x/Al junction extracted from the slope of the measured I - V curve. Because transport is dominated by tunneling through a nanometer-scale amorphous oxide, R_N is exponentially sensitive to the effective barrier transparency. In a simple rectangular-barrier picture,

$$R_N \propto \exp(2\kappa d), \quad \kappa \sim \frac{\sqrt{2mU}}{\hbar}, \quad (2)$$

where d and U denote effective barrier thickness and height, respectively. As a consequence, sub-Ångström changes in the effective barrier thickness (or small changes in the population of locally high-transparency conduction paths) can produce order 10–100% changes in R_N on experimentally relevant timescales. This motivates interpreting the observed resistance drift as a probe of slow, out-of-equilibrium relaxation processes in amorphous AlO_x and its interfaces, rather than requiring large geometric changes of the junction.

A logarithmic time dependence is a common phenomenology for disordered oxide, and can arise from (i) self-limiting thin-oxide growth (e.g., Cabrera-Mott-type kinetics in which the effective driving field across the oxide decreases as the oxide evolves) [27] and/or (ii) “glassy” relaxation with a broad distribution of activation barriers and time constants associated with oxygen vacancies, trapped charge, and local dipoles in amorphous AlO_x [18]. In this work we therefore fit the measured aging curves using a logarithmic form of Eq. 1.

To connect Eq. 1 to a minimal microscopic picture that captures both fabrication and environment effects, we consider two coupled “reservoirs” that control the effective barrier transparency: an internal reservoir (defects and charge configurations within/near the tunnel barrier) and an external reservoir (O/H-containing species that exchange with the environment via exposed Al/AlO_x surfaces and junction edges). We then write the fractional drift as the sum of an intrinsic (environment-insensitive) component and an environment-coupled component,

$$\frac{R_N(t)}{R_0} = 1 + a_{\text{int}} \log\left(1 + \frac{t}{\tau_{\text{int}}}\right) + a_{\text{ext}} \log\left(1 + \frac{t}{\tau_{\text{ext}}(\mathcal{E})}\right), \quad (3)$$

where $R_0 \equiv R_N(t \approx 0)$, \mathcal{E} denotes the storage environment, $a_{\text{int,ext}}$ quantify the available “distance to equilibrium” (set primarily by the as-fabricated defect/inhomogeneity state), τ_{int} describes intrinsic relaxation that persists even in low- p_{O_2} conditions, and $\tau_{\text{ext}}(\mathcal{E})$ captures environment-dependent kinetics associated with O/H exchange. For a fixed environment and over a limited dynamic range, Eq. 3 is well approximated by the single-log fit of Eq. 1, with an effective amplitude $a \approx a_{\text{int}} + a_{\text{ext}}$ and an effective timescale close to the weighted geometric mean

$$\tau_{\text{eff}} \approx \tau_{\text{int}}^{a_{\text{int}}/a} \tau_{\text{ext}}(\mathcal{E})^{a_{\text{ext}}/a}, \quad (4)$$

while the offset parameter b absorbs early-time deviations from the asymptotic logarithm.

Eq. 3 provides a consistent interpretation of the main trends observed in this work. First, the strong separation of the fitted τ between ambient atmosphere, nitrogen glove box, and high vacuum (Fig. 1 and Table II) is naturally captured by $\tau_{\text{ext}}(\mathcal{E})$, since lowering the oxygen and/or water chemical potential suppresses the environment-coupled contribution to the kinetics. Conversely, the observation that the fitted amplitude a varies more strongly between fabrication runs than between storage environments (Table II) is consistent with $a_{\text{int,ext}}$ being set by the as-fabricated distribution of barrier stoichiometry, defect density, and local transparency inhomogeneity (e.g., “hot spots” that dominate conductance and are preferentially modified during subsequent relaxation).

Second, the environment-swapping experiments (Fig. 2) are consistent with changing the boundary condition of the external reservoir: swapping between glove box and atmosphere changes $\tau_{\text{ext}}(\mathcal{E})$ and therefore the apparent aging speed. The slow approach of the resistance trajectory toward the corresponding “bound” curve over several days suggests that equilibration of the internal/external reservoirs is not instantaneous, but limited by diffusion/reaction processes (e.g., incorporation and redistribution of oxygen and/or hydroxyl-related species along junction edges and through near-surface oxide). The small transient “deaging” observed when moving from atmosphere into the glove box after several days can be understood as a partial, reversible relaxation of surface-related contributions (e.g., desorption/dehydration and/or rearrangement of trapped charge and dipoles), which can temporarily increase barrier transparency before the slower intrinsic relaxation dominates.

Third, the alternating-bias voltage annealing results (Table III and Fig. 3), which show an abrupt increase in R for annealed junctions followed by renewed slow drift, can be interpreted within Eq. 3 as a perturbation primarily to the internal reservoir. A voltage pulse of amplitude V_p applied across an oxide of thickness d_{ox} produces an electric field $E \sim V_p/d_{\text{ox}}$ that is large on atomic scales for nanometer-scale oxides. Such fields can drive field-assisted hopping and rearrangement of charged defects

(e.g., oxygen vacancies and trapped charge) in amorphous AlO_x [28], effectively “reconfiguring” the dominant conduction paths and increasing the effective barrier parameter in Eq. 2. In this picture, voltage annealing does not simply accelerate the same environment-driven aging mechanism; rather, it changes the internal configuration (shifting R_0 and/or a_{int}), after which the aging resumes with new initial conditions towards a new “bound” curve.

Finally, the thermal annealing trends (Table IV and Fig. 4) can be understood as the result of competing temperature-activated processes that act on both reservoirs. At elevated temperature, oxygen and defect mobility increase and the oxide can structurally relax on short timescales. In low-oxygen (N_2) anneals, net “barrier softening” processes (defect/charge relaxation and oxygen redistribution that increases transparency) can dominate, yielding a decrease in R , with a larger effect at higher temperature. In ambient atmosphere, additional oxidation/hydroxylation pathways compete with this relaxation and can increase the effective barrier transparency at lower temperature (producing a net increase in R at 200°C), while at higher temperature the transparency-increasing processes can dominate, resulting in a net decrease in R that is partially suppressed compared to N_2 . The inability to reduce R below its initial value is consistent with irreversible removal of the most transparent as-fabricated conduction paths (or irreversible incorporation of oxygen into stable sites), such that annealing can relax the barrier toward a more equilibrated state but cannot fully reconstruct the earliest-time microstructure.

In addition to the mean aging trends, the evolution of junction-to-junction spread (e.g., the CV trends in Fig. 1(b) and Fig. 2(b)) is also qualitatively consistent with Eq. 3: environment-driven contributions are expected to be more heterogeneous (e.g., due to device-to-device variability in edge microgeometry and defect distributions), which can increase the spread in ambient atmosphere, while the predominantly intrinsic component in low-oxygen conditions can yield more stable spreads. Overall, Eq. 3 provides a compact framework to interpret (i) fabrication-dependent aging amplitudes, (ii) environment-dependent aging speeds and swapping behavior, and (iii) voltage/thermal annealing as controlled perturbations to the internal and external relaxation channels.

VI. CONCLUSIONS AND OUTLOOK

In summary, we observed that the logarithmic aging curve of Josephson junction resistances depends on both fabrication conditions and storage conditions. In our case, the difference in oxidation conditions mainly changes the aging amplitude. On the other hand, storage conditions mainly affects aging speed. We found that the effective aging speed in ambient conditions is about 3 to 4 times faster than aging speed in nitrogen environment,

and about 5 times faster than in high vacuum. Swapping between storage conditions show appreciable change in apparent aging speed, with a small deaging when moving from ambient conditions to glove box. We modeled the aging curve to a minimal microscopic picture with both intrinsic and environment-dependent components.

We also compared the effect of voltage and thermal annealing on junctions with identical fabrication but different storage conditions. The similar R change and further aging post-voltage annealing suggest that voltage annealing does not “accelerate” the environmental aging process, but instead changed the internal configuration of the junctions. We observed resistance decrease for thermal annealing in N_2 environment for all temperatures used (up to 250°C). For thermal annealing in ambient conditions, we observed a slight increase at 200°C and decrease at 250°C , suggesting a competition between deaging and aging (e.g oxygen desorption/absorption) processes during annealing.

Even though the resistances were measured in ambient conditions, we expect the added environmental effects during the measurement to be minimal in the aging curve. This is because each measurement time (≈ 20 minutes for a full chip) is much shorter than the time between each measurement (days, up to 1 month). Nevertheless, it might be interesting to compare our results with chips fully stored and measured in the same environment. Additionally, there are additional storage environments of interest, for example: (1) dry cabinet with low ($< 20\%$) relative humidity and near-normal O_2 population, and (2) oxygen-enriched environment with $> 21\%$ O_2 population.

Our results show that to control junction aging, particular care should be taken in junction storage conditions. Uncontrolled storage between qubit junction resistance measurement and cooldown can result in unexpected qubit frequency shift beyond the desired range. While high-vacuum storage resulted in the slowest aging, the large resistance jump we observed after moving the sample out of the vacuum chamber will result in the undesired qubit frequency jump. Instead, the most optimal storage condition appears to be N_2 glove box, with comparable aging speed.

ACKNOWLEDGMENTS

The authors thank Senthil Kumar Karuppanan, Christoph Hufnagel, and Yuanzheng Paul Tan for their assistance and useful discussions, and D. Scott Holmes for valuable suggestions. This project is supported by the National Research Foundation, Singapore through the National Quantum Office, hosted in A*STAR, under its Centre for Quantum Technologies Funding Initiative (S24Q2d0009) and by the National Research Fund (NRF) Quantum Engineering Program (QEP) W21Qpd0211 Advanced Quantum Processor Platform.

- [1] F. Arute, K. Arya, R. Babbush, D. Bacon, J. C. Bardin, R. Barends, R. Biswas, S. Boixo, F. G. S. L. Brandao, D. A. Buell, B. Burkett, Y. Chen, Z. Chen, B. Chiaro, R. Collins, W. Courtney, A. Dunsworth, E. Farhi, B. Foxen, A. Fowler, C. Gidney, M. Giustina, R. Graff, K. Guerin, S. Habegger, M. P. Harrigan, M. J. Hartmann, A. Ho, M. Hoffmann, T. Huang, T. S. Humble, S. V. Isakov, E. Jeffrey, Z. Jiang, D. Kafri, K. Kechedzhi, J. Kelly, P. V. Klimov, S. Knysh, A. Korotkov, F. Kostritsa, D. Landhuis, M. Lindmark, E. Lucero, D. Lyakh, S. Mandrá, J. R. McClean, M. McEwen, A. Megrant, X. Mi, K. Michielsen, M. Mohseni, J. Mutus, O. Naaman, M. Neeley, C. Neill, M. Y. Niu, E. Ostby, A. Petukhov, J. C. Platt, C. Quintana, E. G. Rieffel, P. Roushan, N. C. Rubin, D. Sank, K. J. Satzinger, V. Smelyanskiy, K. J. Sung, M. D. Trevithick, A. Vainsencher, B. Villalonga, T. White, Z. J. Yao, P. Yeh, A. Zalcman, H. Neven, and J. M. Martinis, Quantum supremacy using a programmable superconducting processor, *Nature* **574**, 505 (2019).
- [2] D. Gao, D. Fan, C. Zha, J. Bei, G. Cai, J. Cai, S. Cao, F. Chen, J. Chen, K. Chen, X. Chen, X. Chen, Z. Chen, Z. Chen, Z. Chen, W. Chu, H. Deng, Z. Deng, P. Ding, X. Ding, Z. Ding, S. Dong, Y. Dong, B. Fan, Y. Fu, S. Gao, L. Ge, M. Gong, J. Gui, C. Guo, S. Guo, X. Guo, L. Han, T. He, L. Hong, Y. Hu, H.-L. Huang, Y.-H. Huo, T. Jiang, Z. Jiang, H. Jin, Y. Leng, D. Li, D. Li, F. Li, J. Li, J. Li, J. Li, N. Li, S. Li, W. Li, Y. Li, Y. Li, F. Liang, X. Liang, N. Liao, J. Lin, W. Lin, D. Liu, H. Liu, M. Liu, X. Liu, Y. Liu, Y. Liu, H. Lou, Y. Ma, L. Meng, H. Mou, K. Nan, B. Nie, M. Nie, J. Ning, L. Niu, W. Peng, H. Qian, H. Rong, T. Rong, H. Shen, Q. Shen, H. Su, F. Su, C. Sun, L. Sun, T. Sun, Y. Sun, Y. Tan, J. Tan, L. Tang, W. Tu, C. Wan, J. Wang, B. Wang, C. Wang, C. Wang, C. Wang, J. Wang, L. Wang, R. Wang, S. Wang, X. Wang, X. Wang, X. Wang, Y. Wang, Z. Wei, J. Wei, D. Wu, G. Wu, J. Wu, S. Wu, Y. Wu, S. Xie, L. Xin, Y. Xu, C. Xue, K. Yan, W. Yang, X. Yang, Y. Yang, Y. Ye, Z. Ye, C. Ying, J. Yu, Q. Yu, W. Yu, X. Zeng, S. Zhan, F. Zhang, H. Zhang, K. Zhang, P. Zhang, W. Zhang, Y. Zhang, Y. Zhang, L. Zhang, G. Zhao, P. Zhao, X. Zhao, X. Zhao, Y. Zhao, Z. Zhao, L. Zheng, F. Zhou, L. Zhou, N. Zhou, N. Zhou, S. Zhou, S. Zhou, Z. Zhou, C. Zhu, Q. Zhu, G. Zou, H. Zou, Q. Zhang, C.-Y. Lu, C.-Z. Peng, X. Zhu, and J.-W. Pan, Establishing a new benchmark in quantum computational advantage with 105-qubit Zuchongzhi 3.0 processor, *Phys. Rev. Lett.* **134**, 090601 (2025).
- [3] V. Ambegaokar and A. Baratoff, Tunneling between superconductors, *Phys. Rev. Lett.* **10**, 486 (1963).
- [4] J. B. Hertzberg, E. J. Zhang, S. Rosenblatt, E. Magesan, J. A. Smolin, J.-B. Yau, V. P. Adiga, M. Sandberg, M. Brink, J. M. Chow, and J. S. Orcutt, Laser-annealing Josephson junctions for yielding scaled-up superconducting quantum processors, *npj Quant. Info.* **7**, 129 (2021).
- [5] A. Morvan, L. Chen, J. M. Larson, D. I. Santiago, and I. Siddiqi, Optimizing frequency allocation for fixed-frequency superconducting quantum processors, *Phys. Rev. Res.* **4**, 023079 (2022).
- [6] J. M. Kreikebaum, K. P. O'Brien, A. Morvan, and I. Siddiqi, Improving wafer-scale Josephson junction resistance variation in superconducting quantum coherent circuits, *Supercond. Sci. Tech.* **33**, 06LT02 (2020).
- [7] T. Takahashi, N. Kouma, Y. Doi, S. Sato, S. Tamate, and Y. Nakamura, Uniformity improvement of Josephson-junction resistance by considering sidewall deposition during shadow evaporation for large-scale integration of qubits, *Jpn. J. Appl. Phys.* **62**, SC1002 (2022).
- [8] Y. Zheng, S. Li, Z. Ding, K. Xiong, J. Feng, and H. Yang, Fabrication of Al/AIO_x/Al junctions with high uniformity and stability on sapphire substrates, *Scientific Reports* **13**, 11874 (2023).
- [9] H. Scherer, T. Weimann, A. B. Zorin, and J. Niemeyer, The effect of thermal annealing on the properties of Al–AlO_x–Al single electron tunneling transistors, *J. Appl. Phys.* **90**, 2528 (2001).
- [10] P. J. Koppinen, L. M. Väistö, and I. J. Maasilta, Complete stabilization and improvement of the characteristics of tunnel junctions by thermal annealing, *Appl. Phys. Lett.* **90**, 053503 (2007).
- [11] N. D. Korshakov, D. O. Moskalev, A. A. Soloveva, D. A. Moskaleva, E. S. Lotkov, A. R. Ibragimov, M. V. Androschuk, I. A. Ryzhikov, Y. V. Panfilov, and I. A. Rodionov, Aluminum Josephson junction microstructure and electrical properties modified by thermal annealing, *Scientific Reports* **14**, 26066 (2024).
- [12] E. J. Zhang, S. Srinivasan, N. Sundaresan, D. F. Bogorin, Y. Martin, J. B. Hertzberg, J. Timmerwille, E. J. Pritchett, J.-B. Yau, C. Wang, W. Landers, E. P. Lewandowski, A. Narasgond, S. Rosenblatt, G. A. Keefe, I. Lauer, M. B. Rothwell, D. T. McClure, O. E. Dial, J. S. Orcutt, M. Brink, and J. M. Chow, High-performance superconducting quantum processors via laser annealing of transmon qubits, *Science Advances* **8**, eabi6690 (2022).
- [13] H. Kim, C. Jünger, A. Morvan, E. S. Barnard, W. P. Livingston, M. V. P. Altoé, Y. Kim, C. Song, L. Chen, J. M. Kreikebaum, D. F. Ogletree, D. I. Santiago, and I. Siddiqi, Effects of laser-annealing on fixed-frequency superconducting qubits, *Appl. Phys. Lett.* **121**, 142601 (2022).
- [14] Y. Balaji, N. Acharya, R. Armstrong, K. G. Crawford, S. Danilin, T. Dixon, O. W. Kennedy, R. D. Pothuraju, K. Shahbazi, and C. D. Shelly, *Electron-beam annealing of Josephson junctions for frequency tuning of quantum processors* (2024), arXiv:2402.17395 [quant-ph].
- [15] D. P. Pappas, M. Field, C. J. Kopas, J. A. Howard, X. Wang, E. Lachman, J. Oh, L. Zhou, A. Gold, G. M. Stiehl, K. Yadavalli, E. A. Sete, A. Bestwick, M. J. Kramer, and J. Y. Mutus, Alternating-bias assisted annealing of amorphous oxide tunnel junctions, *Communications Materials* **5**, 150 (2024).
- [16] X. Wang, J. Howard, E. A. Sete, G. Stiehl, C. Kopas, S. Poletto, X. Wu, M. Field, N. Sharac, C. Eckberg, H. Cansizoglu, R. Katta, J. Mutus, A. Bestwick, K. Yadavalli, and D. P. Pappas, Precision frequency tuning of tunable transmon qubits using alternating-bias assisted annealing, in *2024 IEEE International Conference on Quantum Computing and Engineering (QCE)*, Vol. 01 (2024) pp. 1315–1323.
- [17] O. W. Kennedy, J. H. Cole, and C. D. Shelly, Josephson junction tuning described by depinning physics, *Phys. Rev. Lett.* **135**, 196202 (2025).

- [18] J. R. Nesbitt and A. F. Hebard, Time-dependent glassy behavior of interface states in Al-AlO_x-Al tunnel junctions, *Phys. Rev. B* **75**, 195441 (2007).
- [19] C. Križan, M. Toselli, I. Ahmad, H. Khaksaran, M. Rommel, N. Trnjanin, J. Biznárová, M. Dahiya, E. Hogedal, H. Jakobsson, A. Nylander, J. Bylander, P. Delsing, and G. Tancredi, [Electrical post-fabrication tuning of aluminum Josephson junctions at room temperature](#) (2026), [arXiv:2602.20002 \[quant-ph\]](#).
- [20] I. M. Pop, T. Fournier, T. Crozes, F. Lecocq, I. Matei, B. Pannetier, O. Buisson, and W. Guichard, Fabrication of stable and reproducible submicron tunnel junctions, *J. Vacuum Sci. Tech. B* **30**, 010607 (2012).
- [21] A. Bilmes, A. K. Händel, S. Volosheniuk, A. V. Ustinov, and J. Lisenfeld, In-situ bandaged Josephson junctions for superconducting quantum processors, *Supercond. Sci. Tech.* **34**, 125011 (2021).
- [22] J. Van Damme, S. Massar, R. Acharya, T. Ivanov, D. Perez Lozano, Y. Canvel, M. Demarets, D. Vangoidsenhoven, Y. Hermans, J. G. Lai, A. M. Vadiraj, M. Mongillo, D. Wan, J. De Boeck, A. Potočník, and K. De Greve, Advanced CMOS manufacturing of superconducting qubits on 300 mm wafers, *Nature* **634**, 74 (2024).
- [23] D. O. Moskalev, E. V. Zikiy, A. A. Pishchimova, D. A. Ezenkova, N. S. Smirnov, A. I. Ivanov, N. D. Korshakov, and I. A. Rodionov, Optimization of shadow evaporation and oxidation for reproducible quantum Josephson junction circuits, *Scientific Reports* **13**, 4174 (2023).
- [24] N. Muthusubramanian, M. Finkel, P. Duivestein, C. Zachariadis, S. L. M. van der Meer, H. M. Veen, M. W. Beekman, T. Stavenga, A. Bruno, and L. DiCarlo, Wafer-scale uniformity of Dolan-bridge and bridgeless Manhattan-style Josephson junctions for superconducting quantum processors, *Quant. Sci. Tech.* **9**, 025006 (2024).
- [25] C. M. Quintana, A. Megrant, Z. Chen, A. Dunsworth, B. Chiaro, R. Barends, B. Campbell, Y. Chen, I.-C. Hoi, E. Jeffrey, J. Kelly, J. Y. Mutus, P. J. J. O'Malley, C. Neill, P. Roushan, D. Sank, A. Vainsencher, J. Wenner, T. C. White, A. N. Cleland, and J. M. Martinis, Characterization and reduction of microfabrication-induced decoherence in superconducting quantum circuits, *Appl. Phys. Lett.* **105**, 062601 (2014).
- [26] A. Dunsworth, A. Megrant, C. Quintana, Z. Chen, R. Barends, B. Burkett, B. Foxen, Y. Chen, B. Chiaro, A. Fowler, R. Graff, E. Jeffrey, J. Kelly, E. Lucero, J. Y. Mutus, M. Neeley, C. Neill, P. Roushan, D. Sank, A. Vainsencher, J. Wenner, T. C. White, and J. M. Martinis, Characterization and reduction of capacitive loss induced by sub-micron Josephson junction fabrication in superconducting qubits, *Appl. Phys. Lett.* **111**, 022601 (2017).
- [27] N. Cabrera and N. F. Mott, Theory of the oxidation of metals, *Rep. Prog. Phys.* **12**, 163 (1949).
- [28] A. C. Tyner and A. V. Balatsky, [Simulating alternating bias assisted annealing of amorphous oxide tunnel junctions](#) (2025), [arXiv:2512.18420 \[cond-mat.mes-hall\]](#).